



Effect of MgO sintering additive on mullite structures manufactured by fused deposition modeling (FDM) technology

Fateme Sarraf^{a,b,*}, Edoardo Abbatinali^{a,c}, Lovro Gorjan^a, Tutu Sebastian^a, Paolo Colombo^c, Sergey V. Churakov^{b,d}, Frank Clemens^{a,**}

^a Empa-Swiss Federal Laboratories for Materials Science and Technology, 8600, Dübendorf, Switzerland

^b University of Bern, 3012, Bern, Switzerland

^c University of Padova, 35122, Padova, Italy

^d Paul Scherrer Institute, 5232, Villigen, Switzerland

ARTICLE INFO

Keywords:

Fused deposition modeling (FDM)

Mullite

Polymer derived ceramic (PDC)

Polysiloxane

Sintering additive

ABSTRACT

An optimized recipe for 3D printing of Mullite-based structures was used to investigate the effect of MgO sintering additive on the processing stages and final ceramic properties. To achieve dense 3:2 mullite, ceramic filaments were prepared based on an alumina powder, a methyl silicone resin, EVA elastomeric binder and MgO powder. Using 1 wt% MgO and a dwell time of 5 h at 1600 °C, a dense mullite structure could be obtained from filaments with a diameter of 1.75 mm. Ceramic structures with and without sintering additive were printed in vertical and horizontal direction, to investigate the effect of printing direction on mechanical strength after sintering. Using four-point bending test, it was demonstrated that by using MgO, the printing orientation did not affect the mechanical strength significantly anymore. The low Weibull modulus could be explained by the closed porosity that emerge during the degassing of the preceramic polymer due to cross-linking.

1. Introduction

Mullite, e.g. a mixed oxide ceramic based on $3\text{Al}_2\text{O}_3 \cdot 2\text{SiO}_2$, is one of the most commonly used ceramic materials because of its remarkable thermal and mechanical properties [1,2]. The use of mullite in heat protection systems relies on its low thermal conductivity and refractoriness. Moreover, mullite is proposed as a common option for tableware, construction and engineering ceramics, refractories, kiln furniture, substrates for catalytic converters and electronic devices, due to its relatively low thermal expansion coefficient, low creep at high temperatures and associated high thermal shock resistance [3–5]. Considering its low electric conductivity and dielectric constant, mullite can also be employed for electrical insulation applications, for instance, a substrate for electronic devices as well [6].

In the last decade, mullite was investigated additionally for optical, dielectric and structural components, produced using various synthesis and processing strategies. Mullite is a rarely found natural ceramic material, but often it is synthesized using alumina and silica-based raw materials by various methods, such as conventional powder metallurgy

[7], atomic layer deposition (ALD) [8], sol-gel [9–12], co-precipitation [13], combustion [14], chemical vapor deposition (CVD) [15–17] and transient viscous sintering (TVS) [18,19].

Another way to synthesize mullite, by using preceramic polymers, has been investigated by Bernardo et al. in 2006. In this process, the silica that is produced from the decomposition of the preceramic polymer during the thermal heat treatment reacts with alumina powder at 1200–1500 °C [20,21]. The main difficulty in using preceramic polymers for the fabrication of relatively large components is the high mass loss and change in density associated with the polymer to ceramic conversion. This process has a high volume change leading to the formation of pores, blisters and cracks during the pyrolysis process. Using a passive or an active filler, the preceramic polymer content can be reduced, and as a result, the amount of released gaseous by-products and the global shrinkage can be significantly decreased. Passive fillers remain inert during the whole process and do not undergo phase transitions. Those passive fillers neither react with the ceramic residue of the preceramic polymer nor with the gaseous products released during the pyrolysis step. On the contrary, active fillers interact by chemical reaction with the

* Corresponding author at: Empa-Swiss Federal Laboratories for Materials Science and Technology, 8600, Dübendorf, Switzerland.

** Corresponding author.

E-mail addresses: fateme.sarraf@empa.ch (F. Sarraf), frank.clemens@empa.ch (F. Clemens).

<https://doi.org/10.1016/j.jeurceramsoc.2021.06.012>

Received 31 March 2021; Received in revised form 4 June 2021; Accepted 9 June 2021

Available online 11 June 2021

0955-2219/© 2021 The Authors. Published by Elsevier Ltd. This is an open access article under the CC BY license (<http://creativecommons.org/licenses/by/4.0/>).

Table 1

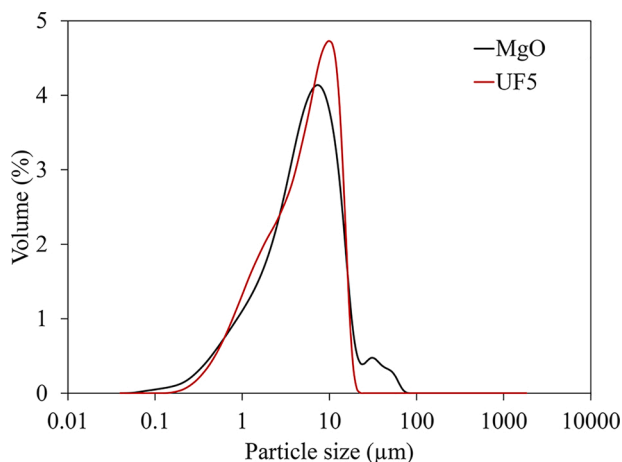
Formulations for ceramic components in the feedstock (i.e. filaments).

Feedstock	UF5 (wt.%)	Silres MK (wt.%)	MgO content in feedstock (wt.%)	MgO content in sintered part (wt.%)
F1	32.47	25.76	0.00	0
FM05	32.34	25.66	0.27	0.5
FM1	32.22	25.57	0.54	1

Table 2

Properties of ceramic components.

		UF5 (γ -Al ₂ O ₃)	MgO
Particle size distribution	D ₁₀ (μ m)	1.11	1.03
	D ₅₀ (μ m)	5.45	5.49
	D ₉₀ (μ m)	13.04	14.90
Specific surface area	SSA (m ² /g)	146.1	30.0
	d _{BET} (μ m)	0.01	0.04
Agglomeration factor	d ₅₀ /d _{BET}	545	137.2
Density	(g/cm ³)	3.95	3.6

**Fig. 1.** Particle size distribution of MgO and Alumina (UF5) powder measured by laser diffraction technique.

preceramic polymer and the gas atmosphere during thermal treatment, compensating for the shrinkage by volume expansion. Greil et al. pioneered this approach, investigating the processing of preceramic polymers containing different intermetallic and metal active fillers [22]. For the synthesis of mullite, active fillers based on metallic aluminum have been already discussed in his paper, the use of alumina powder is an alternative approach investigated by other researchers [20,23–27].

Fused deposition modeling (FDM) was introduced in the 1990s as an additive manufacturing method for ceramics to overcome the practical difficulties of producing ceramic structures with complex geometries and minimize the material waste in comparison to conventional shaping processes [28]. FDM/FFF printing of mullite structures using preceramic polymers has been already reported by Gorjan et al. in 2019, though, full mullite conversion and structure densification could not be achieved at 1550 °C [26].

The Si⁴⁺ and Al³⁺ cations within the mullite lattice show very low bulk and grain-boundary diffusion coefficients. Accordingly, mullite has poor solid-state sinterability, and usually requires high temperatures for densification [29]. To overcome this obstacle, oxides, such as MgO, Y₂O₃ and La₂O₃, have been introduced as sintering aids, among which the MgO has shown the most promising results so far [30]. It has been reported that the sinterability of mullite ceramics can be improved by the formation of a liquid phase in the presence of MgO, which appears in a narrow temperature range, from 1410 to 1425 °C [31]. The enhanced

densification of doped mullite bodies via this mechanism has been also confirmed for industrial mullites. The amount of glassy phase significantly influences the sinterability of mullite, which decreases when the amount of glass phase is reduced [32].

In this paper, we investigated the effect of MgO sintering additive on thermoplastic processing, sinterability, mechanical and microstructural characteristics of filaments and FDM/FFF printed structures derived from preceramic polymer- γ -alumina mixtures, to achieve full mullite transformation and densification. For the first time, a commercial FDM printer has been used to investigate the effect of the printing orientation on the mechanical properties for FDM/FFF printed mullite structures with and without sintering additives, using four-point bending test.

2. Material and methods

2.1. Material

The 3:2 mullite (3Al₂O₃.2SiO₂) was produced using a micron-sized alumina powder (PURALOX SCFa-140 UF5, Sasol Performance Chemicals Ltd) and a methyl silicone resin (Silres MK, Wacker Chemie AG). The Silres MK has a silica yield of approximately 82 wt.% when heated in air at temperatures > ~1000 °C. In addition, magnesium oxide (MgO, Fluka™) was added as a sintering additive. According to the literature [32,33], 0, 0.5 and 1 wt.% of MgO were investigated. An ethylene-vinyl acetate copolymer resin (Elvax 420, Dupont), with a melting point of 73 °C, was employed as a thermoplastic binder for FDM/FFF printing.

The three feedstock formulations used in this study are listed in Table 1. A constant powder content of 40 vol.% was used. Due to the thermoplastic properties of the silicone resin, which has a glass transition temperature in the range of 50–60 °C, the preceramic polymer was treated as a binder with a high ash content after pyrolysis. The powder content of Al₂O₃ and MgO was fixed to a low volume content of 13.8 vol.%.

2.2. Processing

Thermoplastic feedstocks were prepared by mixing all the components in a torque rheometer (Rheomix 600, HAAKE™ PolyLab™ OS, Thermo Fisher Scientific, Germany). Before mixing, the alumina and magnesia powder were dried for 12 h at 110 °C. The mixing was performed for 1 h at 120 °C and 10 rpm using roller rotors. Thermoplastic filaments were fabricated by extrusion through a die with a diameter of 1.8 mm. For the filament fabrication, a capillary rheometer (Rosand RH7, NETZSCH-Gerätebau GmbH, Germany) with a piston speed of 10 mm/min and temperature of 90 °C was used.

The obtained filaments were used for freeform shaping with a commercial FDM/FFF printer (CraftBot2, Craftunique LTD, Hungary). In an FDM printer, the filaments are guided through a roll and a gear wheel that pulls the filament from the spool and pushes it into the heated extrusion nozzle (hot end) with a constant feeding rate. The structure is printed layer by layer on a support according to a 3D model saved as an STL file. In the heated extrusion nozzle, the tip of the filament is melted while the solid part of the filament (outside the hot end) acts as a piston to push the melted part out of the printer head. The printing parameters, optimized by Gorjan et al. in 2019, have been used [26]. The extruder temperature, printing speed, printing angle, nozzle diameter and layer height were set to 170 °C, 7 mm/s, 45°–90°, 0.8 mm and 0.475 mm, respectively.

Thermal processing was carried out in two steps: I) thermal debinding and pre-sintering followed by II) sintering of the filaments and printed samples. Both thermal steps were conducted in a static air atmosphere. For debinding and pre-sintering, a box furnace (Pyrotec PC 12, Michel Keramikbedarf, Switzerland) was used. The filament and printed samples were placed on top of a γ -alumina powder bed covered with a thin layer of carbon black (to avoid sticking to the alumina powder bed) and heated at 1 K/min to 140 °C, then at 0.2 K/min to 230 °C; with an 8 h dwell time at 230 °C. After heating up to 375 °C at a rate of 0.3 K/min, the

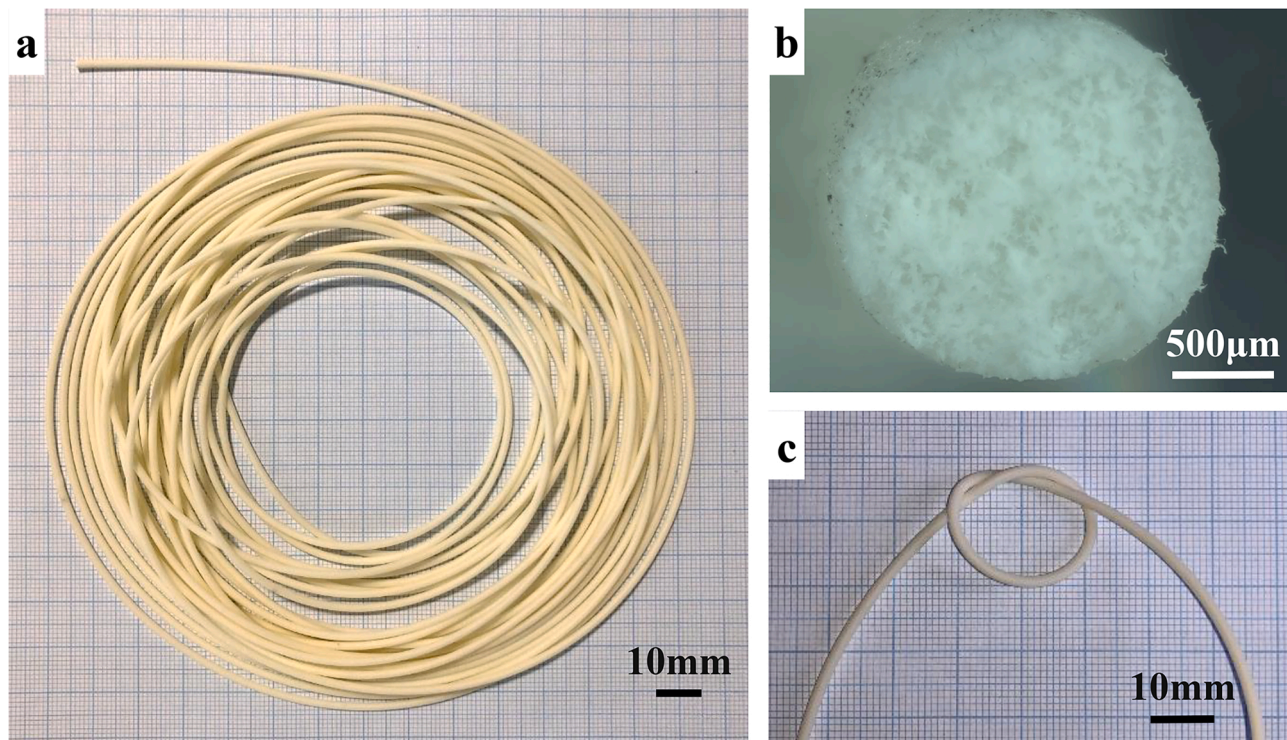


Fig. 2. A spooled filament made from FM1 after extrusion (a) and a cross section of the green filament (b). Flexibility of the filament is demonstrated by tying a knot without filament fracturing (c). (For interpretation of the references to colour in the Figure, the reader is referred to the web version of this article).

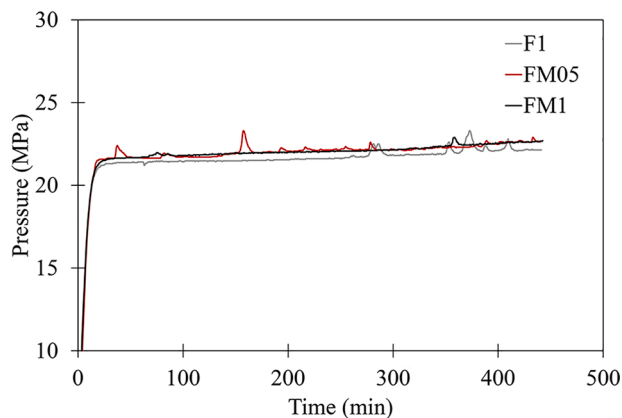


Fig. 3. Pressure versus time plot during the filament extrusion process of the three different feedstocks. The feedstocks were extruded in a capillary rheometer at 90 °C, with a fixed extrusion speed (10 mm/min).

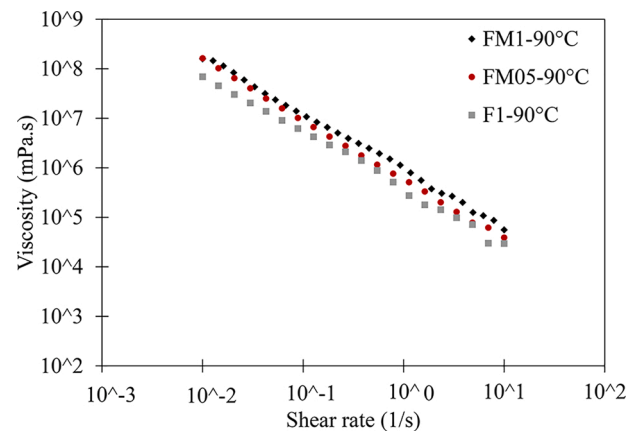


Fig. 4. Viscosity of F1 (0 wt.% MgO), FM05 (0.5 wt.% MgO) and FM1 (1 wt.% MgO) feedstocks, as a function of shear rate at 90 °C, measured by rotational viscosimeter with parallel-plate system.

temperature was held at 375 °C for 10 h. This was followed by an increase in temperature at the same heating rate to 500 °C, then it was raised to 1000 °C at 3 K/min followed by a dwelling time of 2 h at the same temperature. After debinding at 500 °C, the samples were too brittle to handle, and thus pre-sintering up to 1000 °C was required. Sintering of the filaments was carried out in an electrically heated furnace (LHT 03/17 D, Nabertherm GmbH) at 3 K/min to 1600 °C with two different dwell times: 2.5 and 5 h. Based on the results of the firing of the filaments, only a dwell time of 5 h was used for sintering of the 3D printed samples.

2.3. Characterization

Alumina and magnesium oxide powders were analyzed by the gas adsorption method (BET, SA 3100, Beckman Coulter, USA) to determine the specific surface area, and laser diffraction (LS 13 320 XR, Beckman Coulter, USA) to measure the particle size distribution. For the particle

size analysis, the powders were dispersed in distilled water and ultrasonicated for 10 min to break agglomerates.

The d_{BET} is an average diameter calculated from the theoretical density and the measured specific surface area (SSA), assuming that the particles are spherical and monodisperse [34,35]. The d_{BET} can be calculated using Eq. (1):

$$d_{BET} = \frac{6}{SSA \times \rho} \quad (1)$$

The agglomeration factor (d_{50}/d_{BET}) describes the ratio between the measured median particle size by the particle size analyzer and the calculated value obtained from BET (primary particles size). This value can be used to estimate the content of binder that is immobilized in the agglomerates and does not contribute to the plasticization of the feedstock [34,35].

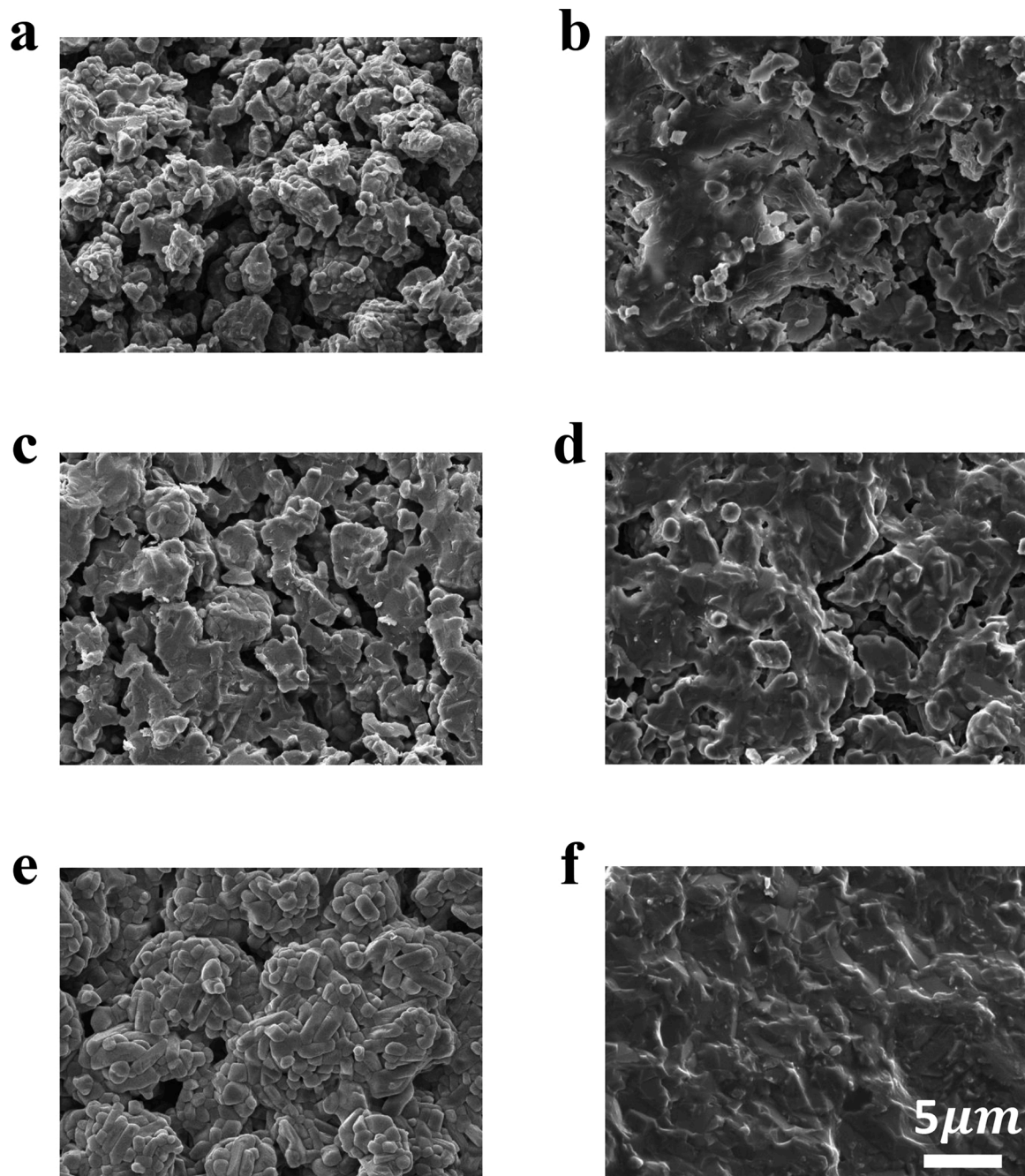


Fig. 5. SEM images of filaments after sintering in air, at 1600 °C for 2.5 (left) and 5 h (right). From the top there are: (a&b) F1, (c&d) FM05 and (e&f) FM1.

To study the microstructure of sintered filaments, the fracture surface of four-point bending test samples, as well as of printed and sintered parts, scanning electron microscopy (SEM, VEGA 3, TESCAN, Czech Republic) was employed. For lower magnifications, an optical stereo microscope (SteREO Discovery.V20, Carl Zeiss AG, Switzerland) was used.

X-ray diffraction analysis (XRD, X'Pert PRO MPD, Malvern Panalytical Ltd, Germany) was carried out between 10–80 degrees at room temperature with a copper anode to evaluate the phase assemblage after sintering of the filaments. The XRD patterns were analyzed using the software (HighScore, Version 4.8, Malvern Panalytical Ltd, Germany).

The pressure during filament fabrication was measured and compared with the viscosity of the feedstocks, measured by a rotational rheometer (MCR 302, Anton Paar, Austria) with a parallel-plate system at 90 °C with a maximal shear rate limited to 10 1/s to avoid draining of the gap.

To investigate the shrinkage and densification of the sintered filaments and specimens, the weight and geometrical size were measured by balance and caliper. Therefore, bulk density- defined as the total mass of a body divided by the geometrical volume- was calculated for 10 samples for each printing configuration.

To evaluate the effect of the printing direction on the mechanical strength of the sintered mullite samples, rectangular specimens were fabricated and four-point flexural strength test was carried out using a universal testing machine (XforceP S/N 760560, ZwickRoell GmbH, Germany). It is worthwhile to mention that only the edges of the specimens were polished (DIN EN 843–1) [36]. It is well-known that the roughness of the first printed layer (in contact with the printing bed) is significantly lower in comparison to the top layer (final layer of the printed structure). Therefore, the specimens were turned for the

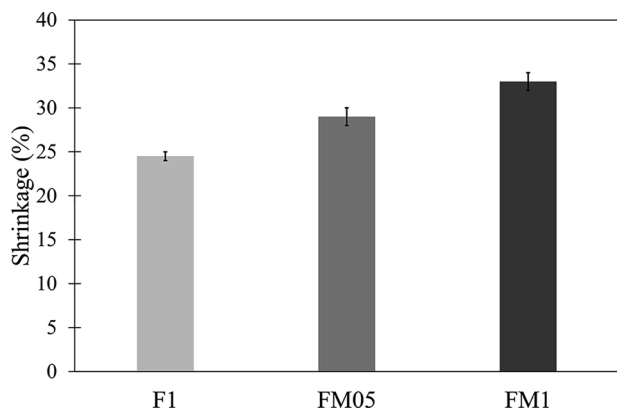


Fig. 6. Mean diameter shrinkage of F1, FM05 and FM1 filaments ($d = 1.75$ mm) after heat-treatment at 1600°C for 5 h of dwell time, in air atmosphere.

four-point bending tests to observe compression mode on the final printed layer.

3. Results

3.1. Materials characterization

The $\gamma\text{-Al}_2\text{O}_3$ (UF5) and MgO ceramic powders were characterized and the results are summarized in Table 2 and Fig. 1.

As can be seen in Table 2, UF5 has a much higher specific surface area. According to the particle size measurement (d_{50}), both powders have a similar particle size distribution (Fig. 1). However, the primary particle size d_{BET} , calculated from the SSA, is 4 times lower for $\gamma\text{-Al}_2\text{O}_3$. This results in a 4 times higher agglomeration factor for the $\gamma\text{-Al}_2\text{O}_3$ powder.

Typically, powder agglomerates break during the high-shear kneading process. If the agglomerates do not break during the compounding step, the internal porous structure will trap some binder. Subsequently, the immobilized binder will not be able to participate efficiently as a plasticizer and only a low ceramic filler content within the thermoplastic polymer can be achieved. Fig. 1 demonstrates the presence of some large agglomerates in the MgO powder ($> 20\ \mu\text{m}$) that could not be destroyed by sonication. While the UF5 presents an asymmetric particle size distribution, with a maximum particle size of $\sim 20\ \mu\text{m}$.

3.2. Fabrication of ceramic-based thermoplastic filaments

Ceramic-based thermoplastic filaments were extruded to be used for the FDM/FFF 3D printing process. The filaments, containing three different amounts of MgO, were flexible enough for spooling and

feeding into a commercial FDM printer. An example of a spooled filament is shown in Fig. 2. A minimal bending radius of 8 mm could be achieved before fracture.

The pressure versus time relations during filament fabrication for the three different feedstocks (0, 0.5 and 1 wt.% of MgO) are shown in Fig. 3. The pressure increase, due to the addition of the sintering additive, was not significant. Therefore, it could be assumed that constant printing parameters for all filaments could be used. However, pressure peaks observed during the filament fabrication (diameter of 1.75 mm) for the F1 composition revealed that agglomerates were still present. Unexpected (see Fig. 1) coarse agglomerates seemed to be formed during the mixing process. Interestingly, building agglomerates could be reduced when introducing MgO, as inferred by the smaller number and magnitude of the pressure peaks in Fig. 3.

In order to prove that the slight increase of the pressure, required during the filament extrusion, was a consequence of viscosity behavior, rotation rheometer experiments were performed using a parallel-plate system (Fig. 4). As expected, the rheological measurements indicated a slight increase in filament viscosity after introducing the MgO sintering aid powder into the feedstock formulation, and all the feedstocks showed a shear thinning behavior.

3.3. Sintering behavior of the thermoplastic filaments

Thermoplastic filaments with different MgO concentrations were sintered in order to investigate the mullite formation and sinterability (e.g. densification). Based on the results of Gorjan et al. [26], the sintering behavior of the filaments was investigated at 1600°C for 2.5 h and 5 h dwell time in air atmosphere. The microstructures of all sintered filaments are shown in Fig. 5.

A dense mullite structure could be obtained by adding MgO and a dwell time of 5 h at 1600°C , as shown in Fig. 5. The calculated shrinkage of the filament diameter, shown in Fig. 6, confirmed the densification process shown by the SEM analysis.

Mullite formation during the sintering was monitored by XRD analysis (see Fig. 7). Free $\gamma\text{-Al}_2\text{O}_3$ could still be observed after 5 h at 1600°C for the filament without MgO. Adding a small amount of MgO (0.5 wt.%), full conversion of mullite could be achieved even after a 2.5 h dwell time. Based on the results, it can be concluded that the MgO sintering additive enables full conversion of the SiO_2 and Al_2O_3 into mullite [37].

3.4. Shrinkage and mechanical properties of 3D printed mullite specimens

To investigate the mechanical properties of the sintered FDM/FFF printed mullite material, rectangular specimens printed in vertical and horizontal orientations were fabricated and tested in a four-point bending configuration. Since 1 wt.% of MgO (FM1) was necessary to

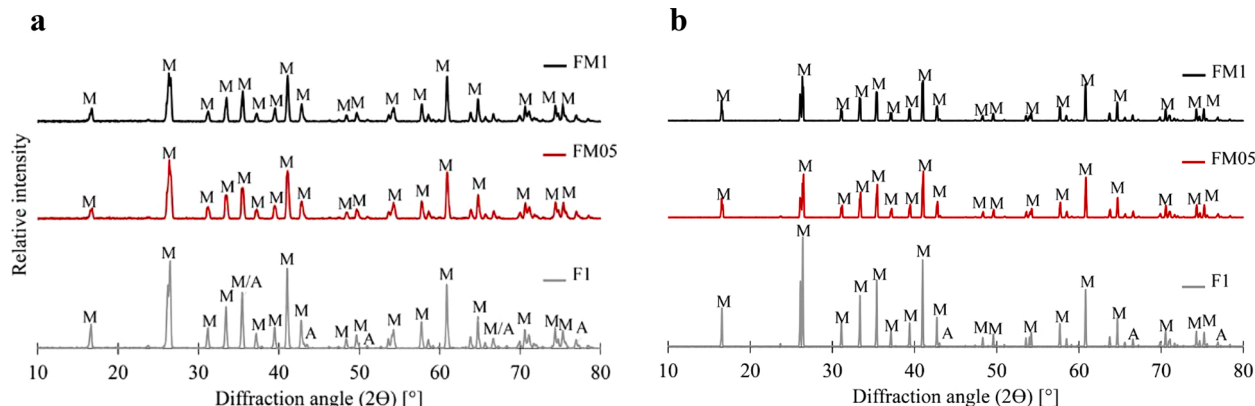


Fig. 7. XRD results comparison between F1 (without MgO), FM05 (0.5 wt.% MgO) and FM1 (1 wt.% MgO) after sintering at 1600°C for (a) 2.5 h and (b) 5 h.

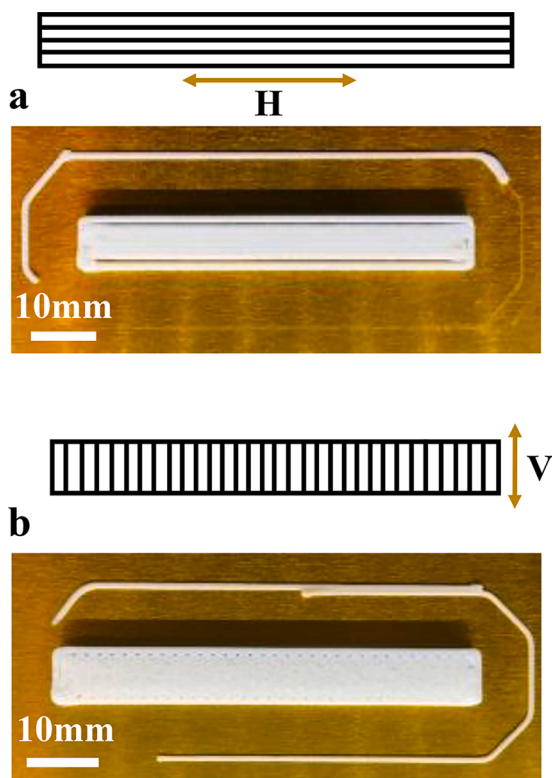


Fig. 8. Printed specimens for mechanical testing. (a) horizontal layout (H) and (b) vertical layout (V). The specimens were cut and polished after printing. Specimen size: 60 mm in length (L), 4.8 mm in width (W) and 3.8 mm in height (H) after printing.

obtain dense microstructure, ceramic specimens for four-point bending test were printed with an infill of 100 % only for the F1 and FM1 formulations (Fig. 8).

The sintered specimens for mechanical testing are shown in Fig. 9-a. Using the measured geometrical values and the weight of the printed and sintered specimens (1600 °C-5 h), their density was calculated (Fig. 9-b). It can be concluded that vertically printed specimens had a

slightly higher green density compared to the horizontally printed ones. However, this effect was neglected after the sintering due to the higher shrinkage and we reached a similar density for both printing orientations.

Based on Fig. 9-b, a density of 1.44 and 2.27 g/cm³ was estimated for the F1 and FM1 sintered specimens, respectively. Since pure mullite has a density of 3.1 g/cm³, highly porous microstructure for the sintered specimens is expected, according to this result. Based on the data, relative density values of 47 % and 73 % were calculated for the F1 and FM1 specimens, respectively.

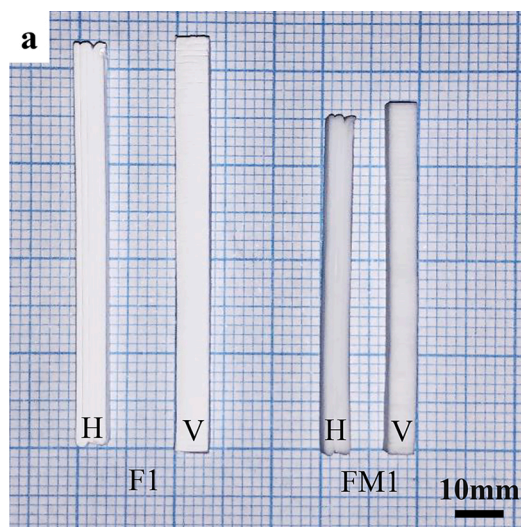
The flexural strength was investigated by four-point bending test, and the Weibull distribution was calculated for all four different specimen configurations: horizontally (H) and vertically (V) printed specimens, with or without MgO.

Obviously, the specimens containing 1 wt.% MgO had higher bending strength compared to those without MgO (Fig. 10). For the specimens without MgO (F1), the mechanical strength between the vertical and horizontal orientation changed significantly, whereas by using 1 wt.% of MgO (FM1), the confidence interval of the horizontal and vertical printed specimens overlapped, and therefore no significant difference could be observed. In general, the mechanical properties of the specimens printed in the vertical orientation were lower than in horizontal orientation. This data can confirm the lower shrinkage and relative density values reported in Fig. 9-b.

3.5. Fractography analysis of FM1 specimens

For fractography analysis, FM1 specimens with the highest mechanical strength were selected, as shown in Fig. 11. The macroporosity was still present in the sintered samples independent of the printing orientations (Fig. 11); however, such structural defects were not present in the green specimens (Fig. 11-a).

The thermal debinding process was investigated by changing different parameters like lower heating rates and longer dwell times to avoid the formation of these pores; however, the phenomena of spherical pores formation could not be solved. Finally, we could prove that the formation of spherical pores happens below the onset temperature of the Silres MK (Fig. 12) that conflicts with the findings of Gorjan et al. in 2019 who investigated the degradation of pure Silres MK and a feed-stock based on Silres MK, γ -Al₂O₃ powder and Elvax420 [26]. Regardless of the material combination, an onset temperature of 170 °C was identified for thermal degradation by TGA analysis.



b

	Density (g/cm ³)		Relative density (%)	Volume shrinkage (%)
	Green	Sintered		
F1H	1.12±0.01	1.48±0.02	48	57
F1V	1.24±0.03	1.44±0.02	47	51
FM1H	1.15±0.02	2.27±0.07	73	71
FM1V	1.20±0.03	2.21±0.08	71	69

Fig. 9. Specimens for mechanical tests after sintering (1600 °C-5 h). (a) F1 and FM1, horizontal (H) and vertical (V) layout, (b) Density and volume shrinkage data calculated for green and sintered printed specimens. (For interpretation of the references to colour in the Figure, the reader is referred to the web version of this article).

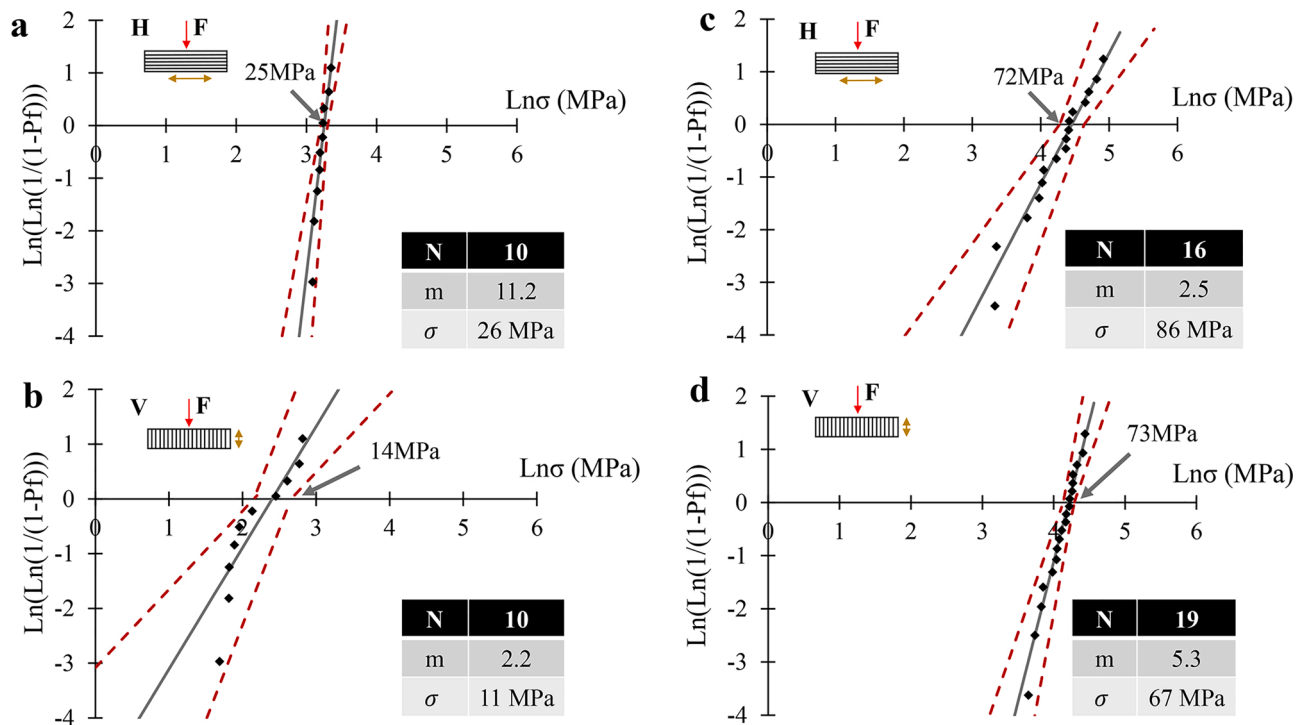


Fig. 10. Weibull distribution of F1 specimens with (a) horizontal and (b) vertical layout and of FM1 specimens with (c) horizontal and (d) vertical layout. N, m and σ represent the number of samples, the Weibull modulus and the average flexural strength value, respectively.

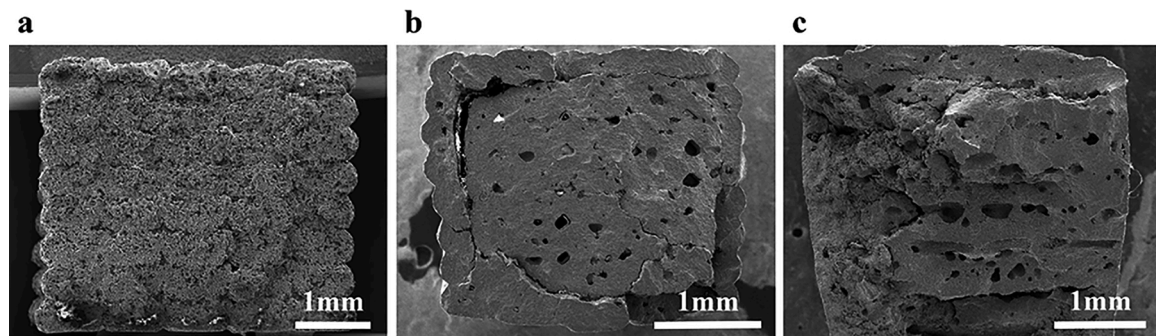


Fig. 11. Fracture surface of (a) green and sintered FM1 specimens (1 wt.% MgO) for (b) horizontal and (c) vertical printing orientations. (For interpretation of the references to colour in the Figure, the reader is referred to the web version of this article).

We posit that the revealed pores below 170 °C are due to the evaporation of water molecules generated by the thermal cross-linking reaction of Silres MK at low temperatures, leading to the condensation of reactive Si–OH groups and release of gas by-products. Indeed, this effect has been exploited for producing SiOC foams through the self-foaming of a similar silicone resin [38]. At temperatures above 73 °C, Elvax 420 starts to melt and subsequently will have high plasticity. Therefore, the released gases during the crosslinking are enclosed and form bubbles instead of cracks. This phenomenon leads to the presence of macro-pores in the microstructure of the final ceramic part. We also observed that the growth of the bubbles depended on the time and temperature the sample was exposed to heat (Fig. 12). Since the decomposition of the Elvax 420 binder starts at higher temperatures (>~240 °C [26]), at which the silicone resin has already mostly undergone thermal cross-linking, we don't expect its decomposition gases to contribute significantly. In addition to the bubble formation, core-shell structure in the SEM image (Fig. 11-b) could be related to the debinding process. In fact, gas species formed during the thermal degradation of the polymeric binder and

pyrolysis of the preceramic polymer will result in high internal stresses for the specimens and cause crack formation.

To investigate the formation of the spherical pores during the debinding process, lightweight sintering substrate with a honeycomb shape was printed.

3.6. FDM printing of honeycomb structures

A lightweight sintering substrates based on a honeycomb structure with a thin bottom layer was printed and sintered (Fig. 13). After the thermal process, the samples retained the shape. As expected, high shrinkage of 37 % and 30 % could be observed for the diameter and the height, respectively.

To investigate the microstructure of the mullite-based substrate, the structure was broken by hand and the fracture surface was analyzed. Fig. 14 shows SEM images of a region connecting the bottom layer and the honeycomb wall. As can be seen, the different printed threads and layers were well diffused. However, macro-pores could be detected in

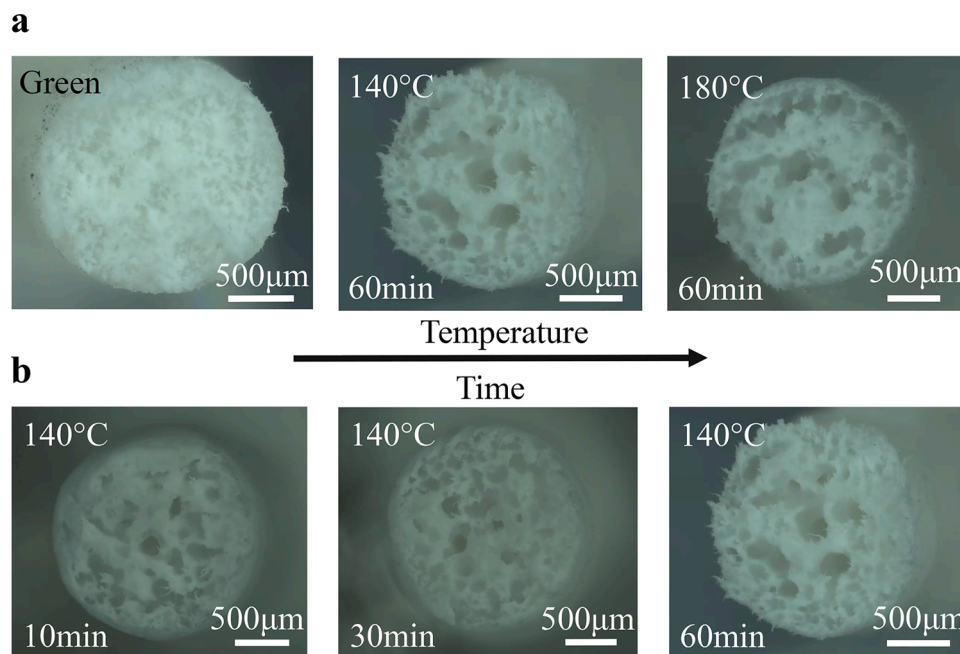


Fig. 12. Optical microscope image for a cross section of FM1 filament in (a) green state and after heat treatment at 140 °C and 180 °C for 60 min, (b) after heat treatment at 140 °C for 10, 30 and 60 min (For interpretation of the references to colour in the Figure, the reader is referred to the web version of this article).

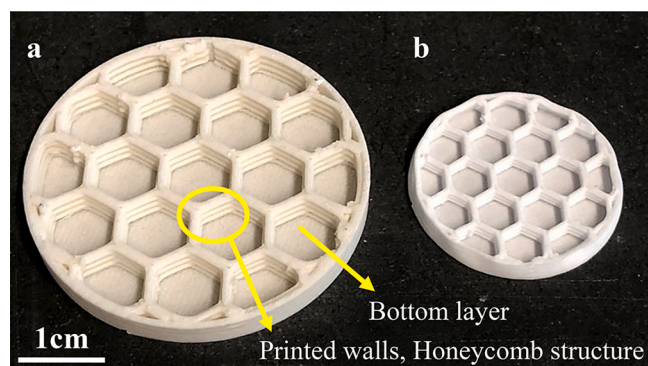


Fig. 13. (a) Green mullite-based lightweight honeycomb substrate with a bottom layer, printed using the FM1 filament, (b) sintered honeycomb substrate at 1600 °C for 5 h. Size after printing: 50 × 10 mm (For interpretation of the references to colour in the Figure, the reader is referred to the web version of this article).

the whole structure, attributable to the evaporation of water molecules as explained above. Nevertheless, the pore size was much smaller than the observed ones in individual filaments or flexural test specimens (see Fig. 11 and 12), and only in some areas with larger wall thickness pores with larger diameter could be detected. Summarizing the observed pore structure present in the lightweight honeycomb substrate and the flexural test specimens, we posit that the wall thickness of the structure will affect the size of the spherical pores. Thus, diffusion of the water molecules through the EVA binder is possible; however, printing of structures with large wall thicknesses should be avoided.

4. Conclusion

In this work, preceramic polymer-based filaments were developed for FDM printing using a combination of a silicone resin and an alumina powder as active filler. Ethylene vinyl acetate was added as thermoplastic

binder to promote the plasticity of the material during extrusion through a hot nozzle.

MgO powder was used as a sintering additive to promote the sinterability and densification of the mullite structures, by forming a liquid phase. Using XRD analysis for the samples with different MgO contents, we demonstrated that only a small amount of MgO (0.5 wt. %) was sufficient to obtain pure mullite after sintering at 1600 °C even with a relatively short dwell time of 2.5 h. However, 1 wt.% of MgO was required to achieve a dense microstructure after sintering at 1600 °C for 5 h.

Although printed samples in horizontal orientation showed a higher green density than the vertical orientation, this effect was neglected after sintering due to higher volume shrinkage. As a result, same sintered density for both orientations was achieved.

Four-point flexural tests were conducted on the specimens with and without 1 wt.% MgO additive to investigate the mechanical properties of the samples printed in the horizontal and vertical orientation. Considering the average flexural strength, we can conclude that the samples with 1 wt.% MgO had higher values, due to the significantly higher densification (e.g. shrinkage) during sintering. Considering the fracture surface of the sintered specimens with 1 wt.% MgO, the low relative density values of the specimens could be explained by the presence of the scattered macro-pores. The formation of pores is attributable to the evaporation of water molecules produced by cross-linking reactions of the Si–OH groups present in the silicon resin. These pores are formed because of the limited diffusion of water molecules through the EVA binder component. Based on these results, we can assume that printing of preceramic-based structures with large wall thickness should be avoided.

Declaration of Competing Interest

The authors declare that they have no known competing financial interests or personal relationships that could have appeared to influence the work reported in this paper.

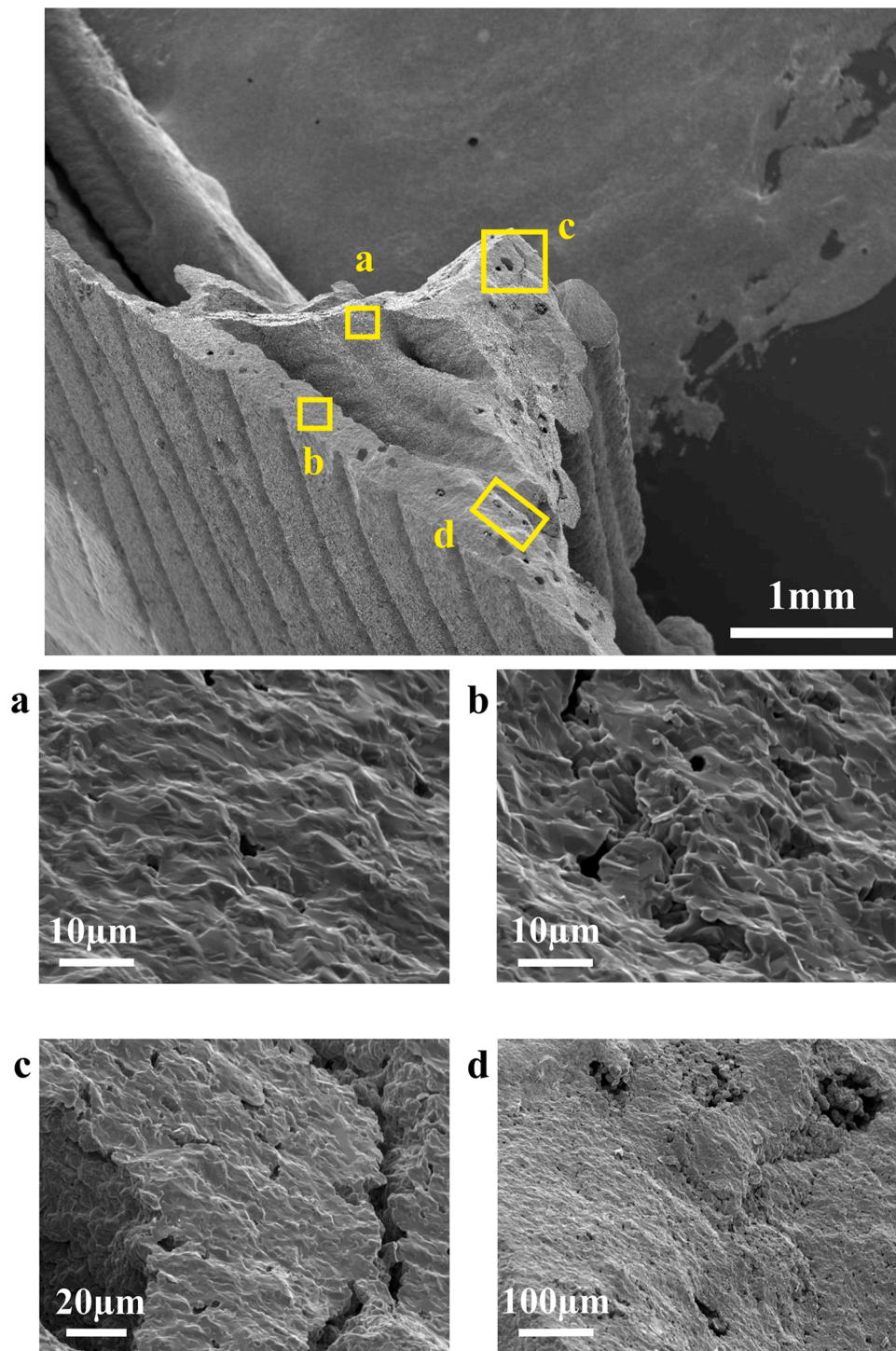


Fig. 14. SEM images of a cross section of the sintered honeycomb substrate, showing the microstructure of both the bottom layer and the honeycomb walls (images taken at different locations).

Acknowledgement

This work was supported by the Swiss National Science Foundation (SNSF) [grant number 200021_184691 / 1].

References

- [1] T. Sato, M. Ishizuka, M. Shimada, Sintering and characterization of mullite—alumina composites, *Ceram. Int.* 12 (1986) 61–65, [https://doi.org/10.1016/0272-8842\(86\)90018-0](https://doi.org/10.1016/0272-8842(86)90018-0).
- [2] H. Schneider, J. Schreuer, B. Hildmann, Structure and properties of mullite—a review, *J. Eur. Ceram. Soc.* 28 (2008) 329–344, <https://doi.org/10.1016/j.jeurceramsoc.2007.03.017>.
- [3] H. Schneider, E. Eberhard, Thermal expansion of mullite, *J. Am. Ceram. Soc.* 73 (1990) 2073–2076, <https://doi.org/10.1111/j.1151-2916.1990.tb05270.x>.
- [4] M. Camerucci, G. Urretavizcaya, M. Castro, A. Cavalieri, Electrical properties and thermal expansion of cordierite and cordierite-mullite materials, *J. Eur. Ceram. Soc.* 21 (2001) 2917–2923, [https://doi.org/10.1016/S0955-2219\(01\)00219-9](https://doi.org/10.1016/S0955-2219(01)00219-9).
- [5] H. Schneider, R.X. Fischer, J. Schreuer, Mullite: crystal structure and related properties, *J. Am. Ceram. Soc.* 98 (2015) 2948–2967, <https://doi.org/10.1111/jace.13817>.

- [6] I.A. Aksay, D.M. Dabbs, M. Sarikaya, Mullite for structural, electronic, and optical applications, *J. Am. Ceram. Soc.* 74 (1991) 2343–2358, <https://doi.org/10.1111/j.1151-2916.1991.tb06768.x> (Aksay et al. 1991).
- [7] T. Huang, M.N. Rahaman, T.I. Mah, T.A. Parthasarathay, Anisotropic grain growth and microstructural evolution of dense mullite above 1550 °C, *J. Am. Ceram. Soc.* 83 (2000) 204–210, <https://doi.org/10.1111/j.1151-2916.2000.tb01171.x>.
- [8] K.P. Furlan, T. Krekeler, M. Ritter, R. Blick, G.A. Schneider, K. Nielsch, R. Zierold, R. Janßen, Low-temperature mullite formation in ternary oxide coatings deposited by ALD for high-temperature applications, *Adv. Mater. Interfaces* 4 (2017) 1700912, <https://doi.org/10.1002/admi.201700912>.
- [9] M. Ismail, H. Tsunatori, Z. Nakai, Preparation of MgO-doped mullite by sol-gel method, powder characteristics and sintering, *J. Mater. Sci.* 25 (1990) 2619–2625, <https://doi.org/10.1007/BF00638068>.
- [10] D. Amutharani, F. Gnanam, Low temperature pressureless sintering of sol-gel derived mullite, *Mater. Sci. Eng. A* 264 (1999) 254–261, [https://doi.org/10.1016/S0921-5093\(98\)01094-6](https://doi.org/10.1016/S0921-5093(98)01094-6).
- [11] M.S. Banu, F. Gnanam, Microstructure and mechanical properties of sol-gel derived mullite containing needle-like grains, *Trans. Indian Ceram. Soc.* 61 (2002) 122–124, <https://doi.org/10.1080/0371750X.2002.10800045>.
- [12] J. Roy, S. Das, S. Maitra, Solgel-processed mullite coating—a review, *Int. J. Appl. Ceram. Technol.* 12 (2015) E71–E77, <https://doi.org/10.1111/ijac.12230> (Roy et al. 2015).
- [13] M. Sanad, M. Rashad, E. Abdel-Aal, M. El-Shahat, Synthesis and characterization of nanocrystalline mullite powders at low annealing temperature using a new technique, *J. Eur. Ceram. Soc.* 32 (2012) 4249–4255, <https://doi.org/10.1016/j.jeurceramsoc.2012.07.014>.
- [14] G.R. Chandran, K. Patil, G. Chandrappa, Combustion synthesis, characterization, sintering and microstructure of mullite-cordierite composites, *J. Mater. Sci. Lett.* 14 (1995) 548–551, <https://doi.org/10.1007/BF00275372>.
- [15] R.P. Mulpuri, V.K. Sarin, Synthesis of mullite coatings by chemical vapor deposition, *J. Mater. Res.* 11 (1996) 1315–1324, <https://doi.org/10.1557/JMR.1996.0166>.
- [16] S. Basu, P. Hou, V. Sarin, Formation of mullite coatings on silicon-based ceramics by chemical vapor deposition, *Int. J. Refract. Metals Hard Mater.* 16 (1998) 343–352, [https://doi.org/10.1016/S0263-4368\(98\)00043-2](https://doi.org/10.1016/S0263-4368(98)00043-2).
- [17] V. Sarin, R. Mulpuri, Chemical Vapor Deposition of Mullite Coatings, Google Patents, 1998.
- [18] M.D. Sacks, N. Bozkurt, G.W. Scheffele, Fabrication of mullite and mullite-matrix composites by transient viscous sintering of composite powders, *J. Am. Ceram. Soc.* 74 (1991) 2428–2437, <https://doi.org/10.1111/j.1151-2916.1991.tb06780.x>.
- [19] M. Bartsch, B. Saruhan, M. Schmücker, H. Schneider, Novel low-temperature processing route of dense mullite ceramics by reaction sintering of amorphous SiO₂-coated γ -Al₂O₃ particle nanocomposites, *J. Am. Ceram. Soc.* 82 (1999) 1388–1392, <https://doi.org/10.1111/j.1151-2916.1999.tb01928.x>.
- [20] E. Bernardo, P. Colombo, E. Pippel, J. Woltersdorf, Novel mullite synthesis based on alumina nanoparticles and a preceramic polymer, *J. Am. Ceram. Soc.* 89 (2006) 1577–1583, <https://doi.org/10.1111/j.1551-2916.2006.00963.x>.
- [21] F. Griggio, E. Bernardo, P. Colombo, G. Messing, Kinetic studies of mullite synthesis from alumina nanoparticles and a preceramic polymer, *J. Am. Ceram. Soc.* 91 (2008) 2529–2533, <https://doi.org/10.1111/j.1551-2916.2008.02515.x>.
- [22] P. Greil, Active-filler-controlled pyrolysis of preceramic polymers, *J. Am. Ceram. Soc.* 78 (1995) 835–848, <https://doi.org/10.1111/j.1151-2916.1995.tb08404.x>.
- [23] D. Suttor, H.J. Kleebe, G. Ziegler, Formation of mullite from filled siloxanes, *J. Am. Ceram. Soc.* 80 (1997) 2541–2548, <https://doi.org/10.1111/j.1151-2916.1997.tb03156.x>.
- [24] R. Riedel, L. Toma, C. Fasel, G. Miehe, Polymer-derived mullite–SiC-based nanocomposites, *J. Eur. Ceram. Soc.* 29 (2009) 3079–3090, <https://doi.org/10.1016/j.jeurceramsoc.2009.05.016>.
- [25] G. Parciannello, *Advanced Ceramics from Preceramic Polymers and Fillers*, PhD thesis, University of Padua, 2012.
- [26] L. Gorjan, R. Tonello, T. Sebastian, P. Colombo, F. Clemens, Fused deposition modeling of mullite structures from a preceramic polymer and γ -alumina, *J. Eur. Ceram. Soc.* 39 (2019) 2463–2471, <https://doi.org/10.1016/j.jeurceramsoc.2019.02.032>.
- [27] J. Schmidt, A.A. Altun, M. Schwenwein, P. Colombo, Complex mullite structures fabricated via digital light processing of a preceramic polysiloxane with active alumina fillers, *J. Eur. Ceram. Soc.* 39 (2019) 1336–1343, <https://doi.org/10.1016/j.jeurceramsoc.2018.11.038>.
- [28] M.K. Agarwala, A. Bandyopadhyay, R. van Weeren, A. Safari, S.C. Danforth, N. A. Langrana, V.R. Jamalabad, P.J. Whalen, FDC, Rapid Fabrication of Structural Components, *American Ceramic Society Bulletin*, 75, 1996.
- [29] Q. Ma, H. Tian, Fabrication and characterization of porous mullite ceramics from pyrolysis of alumina powders filled silicone resin, *J. Wuhan Univ. Technol. Sci Ed* 28 (2013) 1082–1084, <https://doi.org/10.1007/s11595-013-0823-1>.
- [30] V. Viswabaskaran, F. Gnanam, M. Balasubramanian, Effect of MgO, Y₂O₃ and boehmite additives on the sintering behaviour of mullite formed from kaolinite-reactive alumina, *J. Mater. Process. Technol.* 142 (2003) 275–281, [https://doi.org/10.1016/S0924-0136\(03\)00577-6](https://doi.org/10.1016/S0924-0136(03)00577-6).
- [31] L. Montanaro, C. Perrot, C. Esnouf, G. Thollet, G. Fantozzi, A. Negro, Sintering of industrial mullites in the presence of magnesia as a sintering aid, *J. Am. Ceram. Soc.* 83 (2000) 189–196, <https://doi.org/10.1111/j.1151-2916.2000.tb01169.x>.
- [32] P.Md. Souto, R.R. Menezes, R.H.G.A. Kiminami, Evaluation of the influence of MgO and La₂O₃ on the fast sintering of mullite, *Mater. Res.* 18 (2015) 42–53, <https://doi.org/10.1590/1516-1439.264814>.
- [33] L. Montanaro, J. Tulliani, C. Perrot, A. Negro, Sintering of industrial mullites, *J. Eur. Ceram. Soc.* 17 (1997) 1715–1723, [https://doi.org/10.1016/S0955-2219\(97\)00043-5](https://doi.org/10.1016/S0955-2219(97)00043-5).
- [34] J. Heiber, F. Clemens, T. Graule, D. Huelsenberg, Fabrication of SiO₂ {sub 2} glass fibres by thermoplastic extrusion, *Glass Sci. Technol. (Frankfurt)* 77 (2004).
- [35] J. Heiber, F.J. Clemens, T. Graule, D. Hülsenberg, Influence of fibre diameter on the microstructure and the piezoelectric properties of PZT-fibres, *Advances in Science and Technology*, Trans. Tech. Publ. (2006) 2459–2463, <https://doi.org/10.4028/www.scientific.net/AST.45.2459>.
- [36] *Advanced Technical Ceramics - Mechanical Properties of Monolithic Ceramics at Room Temperature - Part 1: Determination of Flexural Strength*; German Version EN 843-1:2006, DIN Deutsches Institut Für Normung e. V., *DIN German Institute for Standardization, 2008, <https://doi.org/10.31030/1457589>, 08.
- [37] M. Ismail, H. Tsunatori, Z. Nakai, Preparation of MgO-doped mullite by sol-gel method, powder characteristics and sintering, *J. Mater. Sci.* 25.5 (1990) 2619–2625, <https://doi.org/10.1007/BF00638068>.
- [38] J. Zeschky, F. Goetz-Neunhoffer, J. Neubauer, S.J. Lo, B. Kummer, M. Scheffler, P. Greil, Preceramic polymer derived cellular ceramics, *Compos. Sci. Technol.* 63 (2003) 2361–2370, [https://doi.org/10.1016/S0266-3538\(03\)00269-0](https://doi.org/10.1016/S0266-3538(03)00269-0).